J. Fluid Mech. (2012), *vol.* 713, *pp.* 307–329.
doi:10.1017/jfm.2012.458

Computations of fully nonlinear hydroelastic solitary waves on deep water

Philippe Guyenne[1] **and Emilian I. Părău**[2]†

[1]Department of Mathematical Sciences, University of Delaware, DE 19716, USA
[2]School of Mathematics, University of East Anglia, Norwich NR4 7TJ, UK

(Received 25 January 2012; revised 20 July 2012; accepted 14 September 2012;
first published online 17 October 2012)

This paper is concerned with the two-dimensional problem of nonlinear gravity waves travelling at the interface between a thin ice sheet and an ideal fluid of infinite depth. The ice-sheet model is based on the special Cosserat theory of hyperelastic shells satisfying Kirchhoff's hypothesis, which yields a conservative and nonlinear expression for the bending force. A Hamiltonian formulation for this hydroelastic problem is proposed in terms of quantities evaluated at the fluid–ice interface. For small-amplitude waves, a nonlinear Schrödinger equation is derived and its analysis shows that no solitary wavepackets exist in this case. For larger amplitudes, both forced and free steady waves are computed by direct numerical simulations using a boundary-integral method. In the unforced case, solitary waves of depression as well as of elevation are found, including overhanging waves with a bubble-shaped profile for wave speeds c much lower than the minimum phase speed c_{min}. It is also shown that the energy of depression solitary waves has a minimum at a wave speed c_m slightly less than c_{min}, which suggests that such waves are stable for $c < c_m$ and unstable for $c > c_m$. This observation is verified by time-dependent computations using a high-order spectral method. These computations also indicate that solitary waves of elevation are likely to be unstable.

Key words: elastic waves, solitary waves, Hamiltonian theory

1. Introduction

In recent years, there has been a growing interest in hydroelasticity problems dealing with the interaction between moving fluids and deformable bodies. Such problems not only entail considerable mathematical challenges but also have many engineering applications (Korobkin, Părău & Vanden-Broeck 2011). An important area of application is that devoted to hydroelastic waves in polar regions where water is frozen in winter and the resulting ice cover is transformed e.g. into roads and aircraft runways, and where air-cushioned vehicles are used to break the ice. A major difficulty in this problem has to do with modelling the ice deformations subject to water wave motions. Theories based on potential flow and on the assumption that the ice cover may be viewed as a thin elastic sheet have been widely used (Squire *et al.* 1996). In this context, most studies have considered linear approximations of the problem, which are valid only for small-amplitude water waves and ice deflections.

† Email address for correspondence: e.parau@uea.ac.uk

Intense waves-in-ice events, however, have also been reported and their analysis indicates that linear theories are not adequate for describing large-amplitude ice deflections (e.g. Marko 2003). In the last few decades, a number of numerical and theoretical investigations have used nonlinear models based on Kirchhoff–Love plate theory to analyse two-dimensional hydroelastic waves in ice sheets. For example, Forbes (1986, 1988) computed periodic finite-amplitude waves using a Fourier series expansion technique. Părău & Dias (2002) derived a forced nonlinear Schrödinger equation for the envelope of ice-sheet deflections due to a moving load, and showed that solitary waves of elevation and depression exist for certain ranges of water depth. Bonnefoy, Meylan & Ferrant (2009) examined numerically the same nonlinear problem of moving loads on ice, through a high-order spectral approach, and found a good agreement with theoretical predictions of Părău & Dias (2002). Hegarty & Squire (2008) simulated the interaction of large-amplitude water waves with a compliant floating raft such as a sea-ice floe, by expanding the solution as a series and evaluating it with a boundary integral method. Vanden-Broeck & Părău (2011) computed periodic waves and generalized solitary waves on deep water using a series truncation method. Milewski, Vanden-Broeck & Wang (2011) considered hydroelastic waves on deep water, in both forced and unforced regimes, with the forced regime being equivalent to a moving load. For the unforced problem, they derived a nonlinear Schrödinger equation which indicates that small-amplitude solitary wavepackets do not exist in the deep-water case. They performed direct time-dependent computations, based on conformal mapping, to verify this prediction. For large amplitudes, their numerical results reveal stable solitary waves of depression coexisting with background radiation. Părău & Vanden-Broeck (2011) addressed the three-dimensional problem in deep water and computed solitary lumps due a steadily moving pressure. However, although they adopted fully nonlinear equations for the fluid, the ice sheet was modelled by the linear Euler–Bernoulli plate.

Recently, Plotnikov & Toland (2011) used the special Cosserat theory of hyperelastic shells, satisfying Kirchhoff's hypothesis and irrotational flow theory, to derive nonlinear equations governing the interaction between a heavy thin elastic sheet and an infinite ocean beneath it. Unlike the Kirchhoff–Love model, this formulation explicitly conserves elastic potential energy. In the present paper, we take advantage of this conservative property to write an explicit Hamiltonian form of the hydroelastic problem in Eulerian coordinates, extending the Hamiltonian formulation of the water wave problem by Zakharov (1968) and Craig & Sulem (1993). We restrict our attention to the deep-water case in two dimensions. The Dirichlet–Neumann operator is introduced to reduce the original Laplace problem to a lower-dimensional system involving quantities evaluated at the fluid–ice interface only.

We first examine the linearized case. Similarly to gravity–capillary water waves, an important property of the hydroelastic problem is that its linear dispersion relation exhibits a minimum c_{min} at which the phase and group velocities coincide. For small- but finite-amplitude waves, we derive a nonlinear Schrödinger equation using the Hamiltonian modulational approach of Craig, Guyenne & Sulem (2010, 2012). The sign of coefficients in this equation suggests that no small-amplitude solitary-wave solutions exist for wave speeds c close to c_{min}. However, we are able to find large-amplitude solitary waves of depression and elevation for $c < c_{min}$, by solving the fully nonlinear steady equations with a boundary integral equation. Similar waves of depression were computed by Milewski *et al.* (2011) using the Kirchhoff–Love model, but these authors did not report results on elevation waves. We also find limiting

configurations in the form of depression overhanging waves with a bubble-shaped profile, when the wave speed is much lower than c_{min}.

In addition, we investigate the spectral stability of these solitary waves by analysing their energy. The presence of an energy minimum at a wave speed c_m slightly less than c_{min} for solitary waves of depression suggests that such waves are (spectrally) stable for $c < c_m$ and unstable for $c > c_m$, as mentioned by e.g. Saffman (1985) for periodic gravity waves on deep water, Milewski, Vanden-Broeck & Wang (2010) for two-dimensional gravity–capillary solitary waves, and Akylas & Cho (2008) for three-dimensional gravity–capillary solitary lumps in a weakly nonlinear model. This stability result inferred from our steady calculations is validated against fully nonlinear time-dependent computations based on the high-order spectral method of Craig & Sulem (1993). Thanks to its analyticity properties, the Dirichlet–Neumann operator has a convergent Taylor series expansion in which each term can be determined recursively. This series expansion combined with the fast Fourier transform lead to an efficient and accurate numerical scheme for solving the full Hamiltonian equations. Our time-dependent computations also indicate that solitary waves of elevation are likely to be unstable.

In the next section, we present the mathematical formulation of the hydroelastic problem and recall linear results. The Dirichlet–Neumann operator is introduced and the Hamiltonian equations of motion are established. From this Hamiltonian formulation, we derive and analyse the nonlinear Schrödinger equation for weakly nonlinear waves in § 3. Section 4 describes the numerical methods developed to solve the full nonlinear problem. In § 4.1, a boundary integral method based on Cauchy's integral formula (Vanden-Broeck & Dias 1992; Vanden-Broeck 2010) is extended to compute forced and free steady waves. In § 4.2, the high-order spectral method of Craig & Sulem (1993) is extended to compute free unsteady waves. Numerical results are shown and discussed in § 5. Finally, concluding remarks are given in § 6.

2. Formulation

2.1. *Equations of motion*

We consider a two-dimensional fluid of infinite depth beneath a thin ice sheet. The ice sheet is modelled using the special Cosserat theory of hyperelastic shells (see Plotnikov & Toland 2011). The fluid is assumed to be incompressible and inviscid, and the flow to be irrotational. We introduce Cartesian coordinates with the x-axis being the bottom of the ice sheet at rest and the y-axis directed vertically upwards. We assume that the fluid surface coincides with the bottom of the ice sheet, so there is no cavitation. The vertical ice sheet deflection is denoted by $y = \eta(x, t)$. The fluid velocity potential $\Phi(x, y, t)$ satisfies the Laplace equation

$$\nabla^2 \Phi = 0 \quad \text{for} \quad -\infty < x < \eta(x, t). \tag{2.1}$$

The nonlinear boundary conditions at $y = \eta(x, t)$ are the kinematic condition

$$\eta_t + \Phi_x \eta_x = \Phi_y, \tag{2.2}$$

and the dynamic condition

$$\Phi_t + \frac{1}{2}(\Phi_x^2 + \Phi_y^2) + g\eta + p(x, t) + \frac{\mathscr{D}}{\rho}\left(\kappa_{ss} + \frac{1}{2}\kappa^3\right) = 0, \tag{2.3}$$

where the subscripts are shorthand notation for partial/variational derivatives (e.g. $\Phi_t = \partial_t \Phi$), κ is the curvature of the fluid–ice interface and s is the arclength along this

interface. In terms of η, the curvature is given by

$$\kappa = \frac{\eta_{xx}}{(1+\eta_x^2)^{3/2}}, \tag{2.4}$$

and therefore

$$\kappa_{ss} + \frac{1}{2}\kappa^3 = \frac{1}{\sqrt{1+\eta_x^2}}\partial_x\left[\frac{1}{\sqrt{1+\eta_x^2}}\partial_x\left(\frac{\eta_{xx}}{(1+\eta_x^2)^{3/2}}\right)\right] + \frac{1}{2}\left(\frac{\eta_{xx}}{(1+\eta_x^2)^{3/2}}\right)^3. \tag{2.5}$$

The system is completed with the condition at infinity

$$\nabla\Phi \to 0 \quad \text{as } y \to -\infty. \tag{2.6}$$

The constant $\mathscr{D}$ is the coefficient of flexural rigidity for the ice sheet, ρ the density of the fluid, g the acceleration due to gravity, and $p(x,t)$ the external pressure distribution exerted on the ice sheet. By definition, if $p > 0$, the pressure acts downwards. The dynamic condition (2.3) is obtained from the Bernoulli equation (see Plotnikov & Toland 2011). The inertia of the thin elastic plate is neglected, so the plate acceleration term is not considered here (see Squire *et al.* 1996). We also assume that the elastic plate is not pre-stressed and neglect the stretching of the plate. It is pointed out that the nonlinear term containing the curvature of the plate in (2.3) is more complex than those used in previous work, which are based on simplified models (see e.g. Forbes 1986; Părău & Dias 2002; Bonnefoy *et al.* 2009; Milewski *et al.* 2011).

If $p = 0$, the total energy

$$H = \frac{1}{2}\int_{-\infty}^{\infty}\int_{-\infty}^{\eta} |\nabla\Phi|^2 \,\mathrm{d}y\,\mathrm{d}x + \frac{1}{2}\int_{-\infty}^{\infty}\left[g\eta^2 + \frac{\mathscr{D}}{\rho}\left(\frac{\eta_{xx}^2}{(1+\eta_x^2)^{5/2}}\right)\right]\mathrm{d}x, \tag{2.7}$$

together with the impulse (or momentum)

$$I = \int_{-\infty}^{\infty}\int_{-\infty}^{\eta} \Phi_x \,\mathrm{d}y\,\mathrm{d}x, \tag{2.8}$$

and the mass (or volume)

$$V = \int_{-\infty}^{\infty} \eta \,\mathrm{d}x, \tag{2.9}$$

are invariants of motion for (2.1)–(2.6). The first integral in (2.7) represents kinetic energy, while the second integral represents potential energy due to gravity and elasticity.

2.2. *Hamiltonian formulation*

In the case $p = 0$, and following Zakharov (1968) and Craig & Sulem (1993), we can reduce the dimensionality of the Laplace problem (2.1)–(2.6) by introducing $\xi(x,t) = \Phi(x,\eta(x,t),t)$, the boundary values of the velocity potential on $y = \eta(x,t)$, together with the Dirichlet–Neumann operator (DNO)

$$G(\eta)\xi = (-\eta_x, 1)^{\top}\cdot\nabla\Phi|_{y=\eta}, \tag{2.10}$$

which is the singular integral operator that takes Dirichlet data ξ on $y = \eta(x,t)$, solves the Laplace equation (2.1) for Φ subject to (2.6), and returns the corresponding Neumann data (i.e. the normal fluid velocity there).

In terms of these boundary variables, (2.1)–(2.3) and (2.6) can be rewritten as

$$\eta_t = G(\eta)\xi, \tag{2.11}$$

$$\xi_t = -\frac{1}{2(1+\eta_x^2)}[\xi_x^2 - (G(\eta)\xi)^2 - 2\xi_x\eta_x G(\eta)\xi] - g\eta - \frac{\mathscr{D}}{\rho}\left(\kappa_{ss} + \frac{1}{2}\kappa^3\right), \tag{2.12}$$

which are Hamiltonian equations for the canonically conjugate variables η and ξ, extending Zakharov's formulation of the water wave problem to hydroelastic waves. Equations (2.11) and (2.12) have the canonical form

$$\begin{pmatrix}\eta_t\\ \xi_t\end{pmatrix} = \begin{pmatrix}0 & 1\\ -1 & 0\end{pmatrix}\begin{pmatrix}H_\eta\\ H_\xi\end{pmatrix}, \tag{2.13}$$

whose Hamiltonian

$$H = \frac{1}{2}\int_{-\infty}^{\infty}\left[\xi G(\eta)\xi + g\eta^2 + \frac{\mathscr{D}}{\rho}\left(\frac{\eta_{xx}^2}{(1+\eta_x^2)^{5/2}}\right)\right]\mathrm{d}x, \tag{2.14}$$

corresponds to the total energy (2.7).

2.3. *Dirichlet–Neumann operator*

In the light of its analyticity properties (Craig, Schanz & Sulem 1997), the DNO can be expressed as a convergent Taylor series expansion

$$G(\eta) = \sum_{j=0}^{\infty} G_j(\eta), \tag{2.15}$$

where each term G_j can be determined recursively (Craig & Sulem 1993; Xu & Guyenne 2009). More specifically, for $j = 2r > 0$,

$$\begin{aligned} G_{2r}(\eta) = {} & \frac{1}{(2r)!}G_0\left(|D|^2\right)^{r-1} D\eta^{2r}D \\ & - \sum_{s=0}^{r-1}\frac{1}{(2(r-s))!}\left(|D|^2\right)^{r-s}\eta^{2(r-s)}G_{2s}(\eta) \\ & - \sum_{s=0}^{r-1}\frac{1}{(2(r-s)-1)!}G_0\left(|D|^2\right)^{r-s-1}\eta^{2(r-s)-1}G_{2s+1}(\eta), \end{aligned} \tag{2.16}$$

and, for $j = 2r-1 > 0$,

$$\begin{aligned} G_{2r-1}(\eta) = {} & \frac{1}{(2r-1)!}\left(|D|^2\right)^{r-1} D\eta^{2r-1}D \\ & - \sum_{s=0}^{r-1}\frac{1}{(2(r-s)-1)!}G_0\left(|D|^2\right)^{r-s-1}\eta^{2(r-s)-1}G_{2s}(\eta) \\ & - \sum_{s=0}^{r-2}\frac{1}{(2(r-s-1))!}\left(|D|^2\right)^{r-s-1}\eta^{2(r-s-1)}G_{2s+1}(\eta), \end{aligned} \tag{2.17}$$

where $D = -\mathrm{i}\partial_x$ and $G_0 = |D|$, so that its Fourier symbol is $|k|$. This formulation, which we used for all of our time-dependent simulations, requires however that η be a single-valued graph of x. As a consequence, the multivalued solutions discussed later were not simulated in time.

2.4. *Linearized problem*

By looking for solutions of the form $\mathrm{e}^{\mathrm{i}k(x-ct)}$ for the linearization of (2.1)–(2.6) with $p=0$ (or equivalently of (2.11)–(2.12)), we obtain the following dispersion relation:

$$c^2=\frac{g}{k}+\frac{\mathscr{D}k^3}{\rho}, \tag{2.18}$$

where c is the phase speed and k the (positive) wavenumber. It can be easily shown that the phase speed $c(k)$ has a minimum c_{min} at $k=k_{min}$ for any values of the parameters (see e.g. Squire *et al.* 1996; Părău & Dias 2002), where

$$k_{min}=\left(\frac{g\rho}{3\mathscr{D}}\right)^{1/4}. \tag{2.19}$$

At this minimum, the phase velocity and the group velocity of the wave are equal, given by

$$c_{min}=\frac{2}{3^{3/8}}\left(\frac{\mathscr{D}g^3}{\rho}\right)^{1/8}. \tag{2.20}$$

3. Nonlinear Schrödinger equation for weakly nonlinear waves

In this section, we analyse the weakly nonlinear regime in the framework of the nonlinear Schrödinger (NLS) equation. For this purpose, we apply the Hamiltonian modulational approach recently developed by Craig *et al.* (2010) to the Hamiltonian formulation (2.11)–(2.14) of the problem. Below we only give a brief description of the derivation of the NLS equation in the present context and refer the reader to Craig *et al.* (2010, 2012) for further details of the method.

3.1. *Canonical transformations*

Changing variables through canonical transformations and expanding the Hamiltonian (2.14) are at the heart of the approach. The first step is a normal mode decomposition defined by

$$\eta=\frac{1}{\sqrt{2}}a^{-1}(D)(z+\bar{z})+\widetilde{\eta},\quad \widetilde{\eta}=\mathbb{P}_0\eta, \tag{3.1a}$$

$$\xi=\frac{1}{\sqrt{2}\mathrm{i}}a(D)(z-\bar{z})+\widetilde{\xi},\quad \widetilde{\xi}=\mathbb{P}_0\xi, \tag{3.1b}$$

where

$$a(D)=\left(\frac{g+\mathscr{D}D^4/\rho}{G_0}\right)^{1/4}, \tag{3.2}$$

and $(\widetilde{\eta},\widetilde{\xi})$ are the zeroth modes representing the mean flow. The overbar represents complex conjugation, and $\mathbb{P}_0$ is the projection that associates to (η,ξ) their zeroth-frequency components. As a result, the canonical system (2.13) is transformed to

$$\begin{pmatrix} z_t\\ \bar{z}_t\\ \widetilde{\eta}_t\\ \widetilde{\xi}_t\end{pmatrix}=\begin{pmatrix} 0 & -\mathrm{i}(\mathbb{I}-\mathbb{P}_0) & 0 & 0\\ \mathrm{i}(\mathbb{I}-\mathbb{P}_0) & 0 & 0 & 0\\ 0 & 0 & 0 & \mathbb{P}_0\\ 0 & 0 & -\mathbb{P}_0 & 0\end{pmatrix}\begin{pmatrix} H_z\\ H_{\bar{z}}\\ H_{\widetilde{\eta}}\\ H_{\widetilde{\xi}}\end{pmatrix}, \tag{3.3}$$

where $\mathbb{I}$ is the identity operator.

The next step introduces the modulational Ansatz

$$z = \varepsilon u(X,t)\mathrm{e}^{\mathrm{i}k_0 x}, \quad \bar{z} = \varepsilon \bar{u}(X,t)\mathrm{e}^{-\mathrm{i}k_0 x}, \tag{3.4}$$

$$\widetilde{\eta} = \varepsilon^3 \widetilde{\eta}_1(X,t), \quad \widetilde{\xi} = \varepsilon^2 \widetilde{\xi}_1(X,t), \tag{3.5}$$

which implies that we look for solutions in the form of quasi-monochromatic waves with carrier wavenumber $k_0 > 0$ and with slowly varying amplitude depending on $X = \varepsilon x$. Wave steepness is measured by the small parameter $\varepsilon = k_0 a_0 \ll 1$ where a_0 is a characteristic wave amplitude. The corresponding equations of motion read

$$\begin{pmatrix} u_t \\ \bar{u}_t \\ \widetilde{\eta}_{1t} \\ \widetilde{\xi}_{1t} \end{pmatrix} = \begin{pmatrix} 0 & -\mathrm{i}\varepsilon^{-1} & 0 & 0 \\ \mathrm{i}\varepsilon^{-1} & 0 & 0 & 0 \\ 0 & 0 & 0 & \varepsilon^{-4} \\ 0 & 0 & -\varepsilon^{-4} & 0 \end{pmatrix} \begin{pmatrix} H_u \\ H_{\bar{u}} \\ H_{\widetilde{\eta}_1} \\ H_{\widetilde{\xi}_1} \end{pmatrix}. \tag{3.6}$$

3.2. *Expansion of the Hamiltonian*

The modulational Ansatz (3.4)–(3.5) also introduces the small parameter ε in the expression of the Hamiltonian (2.14) which can then be expanded in powers of ε. Up to $O(\varepsilon^3)$, we find

$$H = \varepsilon \int_{-\infty}^{\infty} \left[\frac{\bar{u}}{2} \left(\omega(k_0) + \varepsilon \partial_k \omega(k_0) D_X + \frac{\varepsilon^2}{2} \partial_k^2 \omega(k_0) D_X^2 \right) u + \text{c.c.} \right.$$
$$\left. + \frac{\varepsilon^2}{2} \left(\frac{k_0^3}{2} - \frac{5\mathscr{D}k_0^7}{4\rho(g + \mathscr{D}k_0^4/\rho)} \right) |u|^4 \right] \mathrm{d}X + O(\varepsilon^4), \tag{3.7}$$

where c.c. stands for the complex conjugate of all the preceding terms on the right-hand side of the equation, and the coefficient

$$\omega(k) = \sqrt{G_0(g + \mathscr{D}k^4/\rho)} \tag{3.8}$$

denotes the linear dispersion relation in terms of the angular frequency. The scale separation lemma of Craig *et al.* (2005) is used to homogenize the fast oscillations in x and retain the four-wave resonant terms. Note that the mean flow does not contribute to this order of approximation.

The Hamiltonian (3.7) can be further reduced by subtracting a multiple of the conserved wave action

$$M = \varepsilon \int_{-\infty}^{\infty} |u|^2 \, \mathrm{d}X, \tag{3.9}$$

together with a multiple of the conserved impulse

$$I = \int_{-\infty}^{\infty} \eta \xi_x \, \mathrm{d}x = \varepsilon \int_{-\infty}^{\infty} \left[k_0 |u|^2 + \frac{\varepsilon}{2} \left(\bar{u} D_X u + u \overline{D_X u} \right) \right] \mathrm{d}X + O(\varepsilon^5), \tag{3.10}$$

so that the reduced form is

$$\widetilde{H} = H - \partial_k \omega(k_0) I - (\omega(k_0) - k_0 \partial_k \omega(k_0)) M,$$
$$= \frac{\varepsilon^3}{2} \int_{-\infty}^{\infty} \left[\partial_k^2 \omega(k_0) \bar{u} D_X^2 u + \left(\frac{k_0^3}{2} - \frac{5\mathscr{D}k_0^7}{4\rho(g + \mathscr{D}k_0^4/\rho)} \right) |u|^4 \right] \mathrm{d}X + O(\varepsilon^4). \tag{3.11}$$

The subtraction of M from H reflects the fact that our approximation to the problem is phase invariant, while the subtraction of I is equivalent to changing the coordinate system into a reference frame moving with the group velocity $\partial_k\omega(k_0)$. The evolution equation for u is then given by

$$u_t = -\mathrm{i}\widetilde{H}_{\overline{u}}, \tag{3.12}$$

according to (3.6). An advantage of the present approach is that it naturally associates a Hamiltonian to the equations of motion at each order of approximation.

3.3. *Envelope soliton solutions*

Denoting

$$\lambda = \frac{1}{2}\partial_k^2\omega(k_0) = \frac{5\mathscr{D}k_0^3}{\rho\sqrt{gk_0+\mathscr{D}k_0^5/\rho}} - \frac{(g+5\mathscr{D}k_0^4/\rho)^2}{8\,(gk_0+\mathscr{D}k_0^5/\rho)^{3/2}}, \tag{3.13}$$

$$\mu = \frac{5\mathscr{D}k_0^7}{4\rho(g+\mathscr{D}k_0^4/\rho)} - \frac{k_0^3}{2}, \tag{3.14}$$

and rewriting (3.12) more explicitly using (3.11), we obtain the NLS equation

$$\mathrm{i}u_\tau + \lambda\partial_X^2 u + \mu|u|^2 u = 0, \tag{3.15}$$

where $\tau = \varepsilon^2 t$, and the corresponding Hamiltonian is

$$H = \int_{-\infty}^{\infty}\left(\lambda|\partial_X u|^2 - \frac{\mu}{2}|u|^4\right)\mathrm{d}X. \tag{3.16}$$

According to (3.1*a*), the ice-sheet deflection is given in terms of u by

$$\eta(X,\tau) = \frac{\varepsilon}{\sqrt{2}}\left[\left(\frac{|k_0+\varepsilon D_X|}{g+\mathscr{D}\,(k_0+\varepsilon D_X)^4/\rho}\right)^{1/4} u(X,\tau)\mathrm{e}^{\mathrm{i}k_0X/\varepsilon} + \text{c.c.}\right], \tag{3.17}$$

which is accurate up to the order of the NLS equation.

Equation (3.15) is of focusing type, and thus admits soliton solutions travelling at the group velocity $\partial_k\omega(k_0)$, if $\lambda\mu > 0$. Moreover, if $k_0 = k_{min}$, then solitary wavepackets are expected to exist similarly to gravity–capillary waves on deep water (Akylas 1993; Akers & Milewski 2010). These waves have crests which are stationary in the reference frame of their envelopes. Note that we use interchangeably the terminologies 'solitary waves' and 'solitary wavepackets' in the present paper.

Rearranging the expressions of λ and μ, and using the results from § 2.4, we obtain

$$\lambda = \frac{15\,(\mathscr{D}/\rho)^2}{8\,(gk_0+\mathscr{D}k_0^5/\rho)^{3/2}}\left[k_0^4+\left(1+\frac{4}{\sqrt{15}}\right)3k_{min}^4\right]\left[k_0^4+\left(1-\frac{4}{\sqrt{15}}\right)3k_{min}^4\right], \tag{3.18a}$$

$$\mu = \frac{3\mathscr{D}k_0^3/\rho}{4\left(g+\mathscr{D}k_0^4/\rho\right)}\left(k_0^4-2k_{min}^4\right), \tag{3.18b}$$

where k_{min} is given by (2.19). It follows that $\lambda\mu < 0$ if $k_0 = k_{min}$, since

$$\lambda = \left(\frac{3g}{4}\right)^{1/2}\left(\frac{3\mathscr{D}}{g\rho}\right)^{3/8} > 0, \tag{3.19}$$

and

$$\mu = -\frac{3}{16}\left(\frac{g\rho}{3\mathscr{D}}\right)^{3/4} < 0. \tag{3.20}$$

This means that no solitary wavepackets exist for the NLS equation (3.15), which agrees with the NLS results of Milewski *et al.* (2011) based on the Kirchhoff–Love and Cosserat models. This situation may change if finite depth is included in the formulation. For example, Părău & Dias (2002) used a centre manifold and normal form theory for a simplified model to derive a steady NLS equation for weakly nonlinear waves in finite depth, whose coefficients are of the same sign in shallow water, and they showed that solitary wavepackets exist in that case.

It can also be shown that, if

$$k_0 < \left(\frac{12}{\sqrt{15}} - 3\right)^{1/4} k_{min} \approx 0.5601\, k_{min}, \tag{3.21}$$

then both λ and μ are negative, so $\lambda\mu > 0$. Moreover, if

$$k_0 > 2^{1/4} k_{min} \approx 1.1892\, k_{min}, \tag{3.22}$$

then both λ and μ are positive, so $\lambda\mu > 0$ as well. The latter two focusing cases however imply that there is a phase shift between the carrier and envelope peaks, and they were not observed in our numerical simulations.

4. Numerical methods

Following Takizawa (1985), Bonnefoy *et al.* (2009) and Milewski *et al.* (2011), we non-dimensionalize (2.1)–(2.6) using the characteristic scales

$$l = \left(\frac{\mathscr{D}}{\rho g}\right)^{1/4}, \quad v = \left(\frac{\mathscr{D} g^3}{\rho}\right)^{1/8}, \tag{4.1}$$

as unit length and unit velocity, respectively. In non-dimensional form, these equations read

$$\nabla^2 \Phi = 0 \quad \text{for } -\infty < x < \eta(x,t), \tag{4.2}$$

$$\eta_t + \Phi_x \eta_x = \Phi_y \quad \text{for } y = \eta(x,t), \tag{4.3}$$

$$\Phi_t + \tfrac{1}{2}(\Phi_x^2 + \Phi_y^2) + \eta + P + \kappa_{ss} + \tfrac{1}{2}\kappa^3 = 0 \quad \text{for } y = \eta(x,t), \tag{4.4}$$

$$\boldsymbol{\nabla}\Phi \to 0 \quad \text{as } y \to -\infty. \tag{4.5}$$

The localized pressure distribution is assumed to be of the form

$$P = P_0 \mathrm{e}^{-(x-ct)^2/16}, \tag{4.6}$$

as in Milewski *et al.* (2011), but it can be easily replaced with other formulae. When calculating free steady waves, we set $P_0 = 0$. The parameter which will be varied in the problem is c, the non-dimensional wave speed. Note that the non-dimensional minimum phase velocity is

$$c_{min} = \frac{2}{3^{3/8}} \approx 1.324675. \tag{4.7}$$

Our methods to compute steady and unsteady waves are based on boundary-integral and high-order spectral methods, respectively. They are presented separately in the following sections.

4.1. *Boundary-integral method for steady waves*

As we are looking for steady wave solutions of (4.2)–(4.5), we choose a frame of reference moving with the wave speed c. We define $\hat{x} = x - ct$ and introduce

$$\hat{\Phi}(\hat{x}, y) = \Phi(x, y, t) - c\hat{x}, \quad \hat{\eta}(\hat{x}) = \eta(x, t). \tag{4.8}$$

Dropping the hats, the boundary conditions at the fluid–ice interface become

$$\Phi_x \eta_x = \Phi_y, \tag{4.9}$$

$$\tfrac{1}{2}(\Phi_x^2 + \Phi_y^2 - c^2) + \eta + P + \kappa_{ss} + \tfrac{1}{2}\kappa^3 = 0. \tag{4.10}$$

The problem is solved numerically using a boundary-integral-equation technique based on Cauchy's integral formula (see Vanden-Broeck & Dias 1992; Vanden-Broeck 2010). The complex potential

$$w(z) = \Phi(x, y) + \mathrm{i}\,\Psi(x, y) \tag{4.11}$$

is introduced in the fluid domain, where $\Psi(x, y)$ is the stream function. The physical plane

$$z = x(w) + \mathrm{i}\,y(w) \tag{4.12}$$

is mapped to $w(z)$ in the inverse plane. Therefore

$$\Phi_x - \mathrm{i}\,\Phi_y = \frac{\mathrm{d}w}{\mathrm{d}z} = \frac{1}{x_\Phi + \mathrm{i}\,y_\Phi}. \tag{4.13}$$

Without loss of generality, we set $\Psi = 0$ on the elastic sheet/fluid interface and choose $\Phi = 0$ at $x = 0$. In terms of the potential, the elastic sheet/fluid interface profile is denoted by $(x(\Phi), y(\Phi)) = (x(\Phi + \mathrm{i}\,0), y(\Phi + \mathrm{i}\,0))$. In this notation, $x'(\Phi)$ and $y'(\Phi)$ are the values of x_Φ and y_Φ evaluated at the interface $\Psi = 0$.

Assuming the symmetry of solutions about $\Phi = 0$, application of the Cauchy integral formula to a large semicircle in the fluid layer yields, after some algebra,

$$x'(\Phi_0) - \frac{1}{c} = -\frac{1}{\pi} \fint_0^\infty y'(\Phi) \left(\frac{1}{\Phi - \Phi_0} + \frac{1}{\Phi + \Phi_0} \right) \mathrm{d}\Phi, \tag{4.14}$$

where the primes denote differentiation with respect to Φ. The evaluation point Φ_0 lies on the interface and the integral on the right-hand side is evaluated in the principal value sense.

The dynamic condition (4.10) becomes in the inverse plane

$$\frac{1}{2}\left(\frac{1}{x'^2 + y'^2} - c^2 \right) + y + P + \frac{1}{2}\left(\frac{y''x' - y'x''}{(x'^2 + y'^2)^{3/2}} \right)^3 + \frac{S}{(x'^2 + y'^2)^{9/2}} = 0, \tag{4.15}$$

where

$$\begin{aligned} S = {} & x'^5 y^{(\mathrm{iv})} + 2x'^3 y'^2 y^{(\mathrm{iv})} + x' y'^4 y^{(\mathrm{iv})} - 6x'^4 x'' y''' - 2x'^2 y'^2 x'' y''' \\ & + 4x'' y'^4 y''' - x'^4 x^{(\mathrm{iv})} y' - 2x'^2 x^{(\mathrm{iv})} y'^3 - x^{(\mathrm{iv})} y'^5 - 4x'^4 x''' y'' \\ & + 2x'^2 x''' y'^2 y'' + 6x''' y'^4 y'' - 10x'^3 y' y'' y''' + 10x'^3 x'' x''' y' \\ & + 10x' x'' x''' y'^3 - 10x' y'^3 y'' y''' - 39x' x''^2 y'^2 y'' + 3x''^3 y'^3 - 3x'^3 y''^3 \\ & + 15x' y'^2 y''^3 + 39x'^2 x'' y' y''^2 - 15x'' y'^3 y''^2 + 15x'^3 x''^2 y'' - 15x'^2 x''^3 y'. \end{aligned} \tag{4.16}$$

We should note that this formulation of the problem can be derived without assuming that the interface is single-valued. It allows us to compute waves with multivalued profiles, as the surface is given in parametric form $(x(\Phi), y(\Phi))$. We choose the pressure to be of the form $P(\Phi) = P_0 \mathrm{e}^{-\Phi^2/16}$, where $P_0 = 0$ and $P_0 \neq 0$ when computing free and forced waves, respectively.

Equations (4.14) and (4.15) define a system for the unknown functions $x(\Phi)$ and $y(\Phi)$ which is solved by employing a method that extends the one described in Vanden-Broeck & Dias (1992). The system is discretized by choosing n equally spaced points $\Phi_j = j\Delta\Phi$ for $j = 1, \ldots, n$. The integral (4.14) is evaluated at mid-points by the trapezoidal rule. Finite differences and interpolation formulae are used for the derivatives. Equation (4.15) is evaluated at the interior grid points, and a symmetry condition at Φ_1 together with a truncation condition at Φ_n are imposed. The nonlinear system obtained for the unknowns $y_i' = y'(\Phi_i)$, where $i = 1, \ldots, n$, is solved by Newton's method.

We checked the accuracy of the method by varying the number of points and the grid interval. The truncation error was also monitored by varying the length of the whole integration interval. If this interval is long enough, the truncation affects only the last few points and is noticeable only when c is very close to c_{min}. Most steady results presented here are obtained with $n = 3200$ and $\Delta\Phi = 0.025$, and they are unchanged within graphical accuracy if the grid spacing is decreased (or the number of points is increased). However for limiting cases when c is small, a finer grid interval was needed and we used $\Delta\Phi = 0.0125$ or 0.00625.

4.2. *High-order spectral method for unsteady waves*

To compute unsteady waves, we solve numerically the Hamiltonian equations (2.11)–(2.12) in space and time (Craig & Sulem 1993; Guyenne & Nicholls 2007). For space discretization, we assume periodic boundary conditions in x, with $0 \leqslant x \leqslant L$, and use a pseudospectral method based on the fast Fourier transform. This is a particularly suitable choice for the computation of the DNO since each term in its Taylor series expansion (2.15)–(2.17) consists of concatenations of Fourier multipliers with powers of η.

More specifically, both functions η and ξ are expanded in truncated Fourier series:

$$\begin{pmatrix} \eta \\ \xi \end{pmatrix} = \sum_{\mathrm{k}} \begin{pmatrix} \widehat{\eta}_k \\ \widehat{\xi}_k \end{pmatrix} \mathrm{e}^{\mathrm{i}kx}. \tag{4.17}$$

Spatial derivatives and Fourier multipliers are evaluated in the Fourier domain, while nonlinear products are calculated in the physical domain on a regular grid of N collocation points. For example, if we wish to apply the zeroth-order operator G_0 to a function ξ in the physical domain, we transform ξ to the Fourier domain, apply the diagonal operator $|k|$ to the Fourier coefficients of ξ, and then transform back to the physical domain. In practice, the Taylor series of the DNO is also truncated to a finite number of terms,

$$G(\eta) \approx \sum_{j=0}^{J} G_j(\eta), \tag{4.18}$$

and thanks to its analyticity properties, a small number of terms (typically $J < 10$) is sufficient to achieve very accurate results (Xu & Guyenne 2009). Aliasing errors are removed by zero-padding in the Fourier domain (Canuto *et al.* 1987).

Time integration of (2.11) and (2.12) is performed in the Fourier domain so that the linear terms can be solved exactly by the integrating-factor technique. The nonlinear terms are integrated in time using a fourth-order Runge–Kutta scheme with constant time step Δt. For this purpose, we separate the linear and nonlinear parts of (2.11)–(2.12). Defining $\boldsymbol{v} = (\eta, \xi)^{\top}$, these equations (in dimensionless form) can be rewritten as

$$\boldsymbol{v}_t = \mathscr{L}(\boldsymbol{v}) + \mathscr{N}(\boldsymbol{v}), \tag{4.19}$$

where the linear part $\mathscr{L}(\boldsymbol{v})$ is defined by

$$\mathscr{L}(\boldsymbol{v}) = \begin{pmatrix} 0 & G_0 \\ -1 - \partial_x^4 & 0 \end{pmatrix} \begin{pmatrix} \eta \\ \xi \end{pmatrix}, \tag{4.20}$$

and the nonlinear part $\mathscr{N}(\boldsymbol{v})$ is defined by

$$\mathscr{N}(\boldsymbol{v}) = \begin{pmatrix} (G(\eta) - G_0)\xi \\ -\dfrac{1}{2(1+\eta_x^2)}[\xi_x^2 - (G(\eta)\xi)^2 - 2\xi_x\eta_x G(\eta)\xi] - \kappa_{ss} - \frac{1}{2}\kappa^3 + \eta_{xxxx} \end{pmatrix}. \tag{4.21}$$

Further details on how $\mathscr{L}(\boldsymbol{v})$ and $\mathscr{N}(\boldsymbol{v})$ come into play in the time-integration scheme can be found in Xu & Guyenne (2009). The addition and subtraction of η_{xxxx} in (4.20)–(4.21) help minimize the stiffness due to flexural rigidity. If specified, the pressure term is added to the second line in (4.21).

In computations of large-amplitude or steep waves, we observed that spurious high-wavenumber modes can develop in the wave profile after some time of integration. This difficulty is likely to be due to the nonlinearity and stiffness of the problem that promote the growth of numerical errors, and it may require use of prohibitively small time steps to ensure stability. As a remedy, we applied an ideal low-pass filter at each time step to $\widehat{\eta}_k$ and $\widehat{\xi}_k$, in the form

$$\gamma(k) = \begin{cases} 1 & \text{if } |k|/k_{\max} \leqslant \nu, \ 0 < \nu \leqslant 1, \\ 0 & \text{if } |k|/k_{\max} > \nu, \end{cases} \tag{4.22}$$

where $k_{\max}$ is the largest wavenumber of the spectrum. We typically found that $\nu = 0.8$ suffices to stabilize the numerical solution. Care was taken to specify a sufficiently fine spatial resolution so that only energy levels at high wavenumbers are suppressed by filtering.

Starting from zero initial conditions, free solitary waves are produced by applying the pressure (4.6) over a finite interval of time $0 \leqslant t \leqslant T$, with given P_0 and c. The pressure distribution is initially centred at $x = L/2$. To minimize the generation of radiation due to a cold start, we also apply a tanh-like ramp function in time to (4.6), which allows a smooth transition from 0 to P_0 (Guyenne & Nicholls 2007). Despite our effort however, small radiative waves were inevitably excited by the applied pressure in our numerical simulations. A typical run uses $J = 6$, $\Delta t = 0.002$ and $N = 4096$ for a computational domain of length $L = 600$. These values of numerical parameters were found to be a good compromise between accuracy and computational cost. Numerical tests on the conservation of invariants of motion will be shown in the next section.

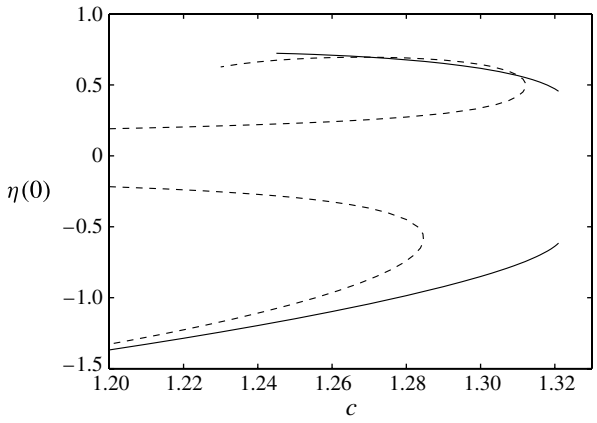

FIGURE 1. Amplitudes of free (solid line) and forced (dashed line) solitary waves. $P_0 = 0.1$ for the forced depression branch ($\eta(0) < 0$) and $P_0 = -0.1$ for the forced elevation branch ($\eta(0) > 0$).

5. Numerical results

5.1. *Steady waves*

We first computed forced solitary waves for $c < c_{min}$. Both depression and elevation forced waves were found, depending on the sign of P_0. Based on a continuation method developed before (e.g. Vanden-Broeck & Dias 1992), by removing gradually the pressure when c is close to c_{min}, we were able to compute branches of depression and elevation free solitary waves.

Amplitudes of free and forced solitary waves as functions of c are presented in figure 1. The branches of forced waves do not exist up to c_{min}, but only to some value c_{P_0} smaller than c_{min} when P_0 is large. For each value of $c < c_{P_0}$, there are two forced solutions, one being a perturbation of the uniform flow, the other being a perturbation of the solitary wave. The waves are of elevation when P_0 is negative and of depression when P_0 is positive. The turning point of the elevation forced solitary waves branch is closer to c_{min} than the turning point of the depression forced solitary waves branch for pressures having the same magnitude but opposite sign. For speeds between c_{P_0} and c_{min}, there are no steady solutions (see also Milewski *et al.* 2011). The turning point of the branches, c_{P_0}, increases with decreasing $|P_0|$ until it equals c_{min}. When $|P_0|$ is small, we observed that the two branches of forced solitary waves can be followed up to c_{min} where they end at finite amplitudes.

It can be observed from figure 1 that the branches of free solitary waves start at a finite amplitude, when $c \approx c_{min}$. Examples of free solitary waves are presented in figures 2 and 3. The number and amplitude of oscillations in both forced and free solitary waves increase as c approaches c_{min}. As c decreases, the amplitude of the depression solitary wave increases and only one large peak is observed, followed by a small elevation crest (see figure 2). The branch of elevation solitary waves can be followed only to some point, which indicates the possible existence of a turning point. The central peak of the elevation solitary wave becomes smaller in absolute value than the neighbouring troughs (see figure 3).

As the amplitude of the depression wave increases and the speed c decreases past a value of around 0.8, the solutions exhibit overhanging profiles (see figure 4*a*). A similar phenomenon was observed by Vanden-Broeck & Părău (2011) for periodic

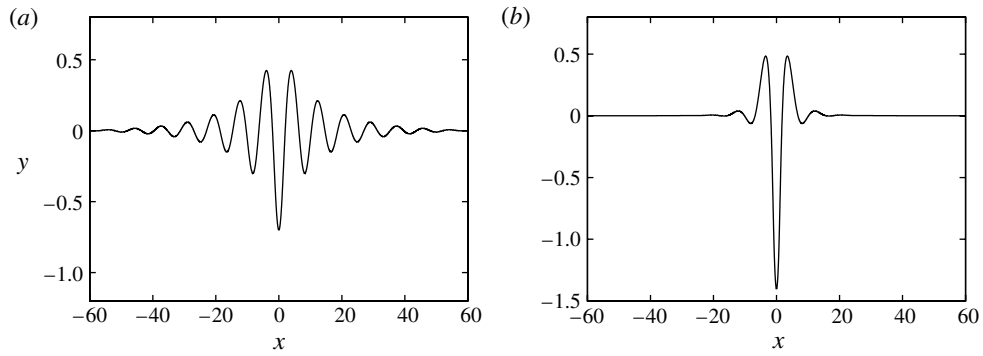

FIGURE 2. Examples of free depression solitary waves: (*a*) $c = 1.316$; (*b*) $c = 1.192$.

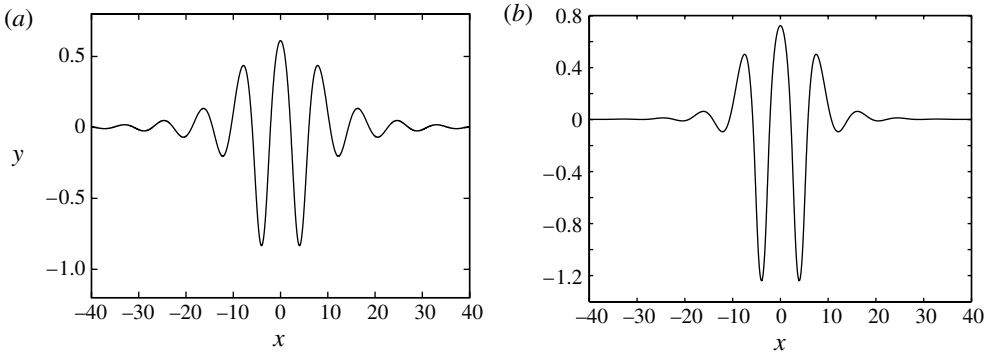

FIGURE 3. Examples of free elevation solitary waves: (*a*) $c = 1.301$; (*b*) $c = 1.245$.

hydroelastic waves in a simplified model. For capillary and gravity–capillary waves, this is a well-known phenomenon, when the limiting configuration is a wave with a trapped bubble at its trough (see Crapper 1957 for periodic capillary waves and Vanden-Broeck & Dias 1992 for gravity–capillary solitary waves). It is worth noting that Blyth, Părău & Vanden-Broeck (2011) discovered the limiting configuration for periodic nonlinear hydroelastic waves between fluid sheets (when gravity is neglected) to correspond to a static profile of the elastic plates. In our case, the limiting case of the branch is a solution with a trapped bubble at some small value of c. We could not follow the branch up to this point, as the convergence of the numerical scheme becomes increasingly difficult to achieve for values of c smaller than 0.15. However, in the limit $c \to 0$, there is no flow in the fluid and (4.4) can be rewritten in the form

$$y(s) + \kappa_{ss} + \tfrac{1}{2}\kappa^3 = 0. \tag{5.1}$$

Equation (5.1), together with the equations $x_{ss} = -\kappa\, y_s$ and $y_{ss} = \kappa\, x_s$, are integrated numerically by rewriting them as a first-order system and using a Runge–Kutta method (see Blyth *et al.* 2011).

The so-obtained solution is singular with a self-intersecting profile, which is unrealistic (see figure 4*b*). This solution is the limit of the branch of computed solitary waves as $c \to 0$, which means that singular waves with self-intersecting profiles exist for small values of c, but obviously they have no physical meaning. The possible

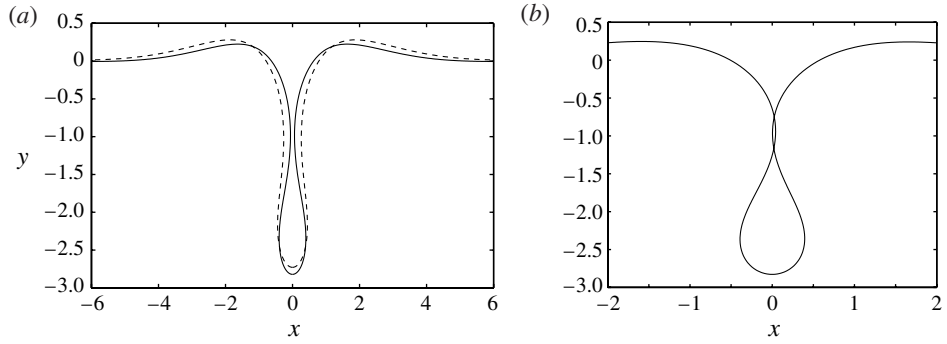

FIGURE 4. (*a*) Examples of large-amplitude solitary waves with overhanging profiles. The values of c are 0.187 (solid line) and 0.475 (dashed line). Only the central part of the wave is shown. (*b*) Profile of the singular solution with self-intersection for $c = 0$.

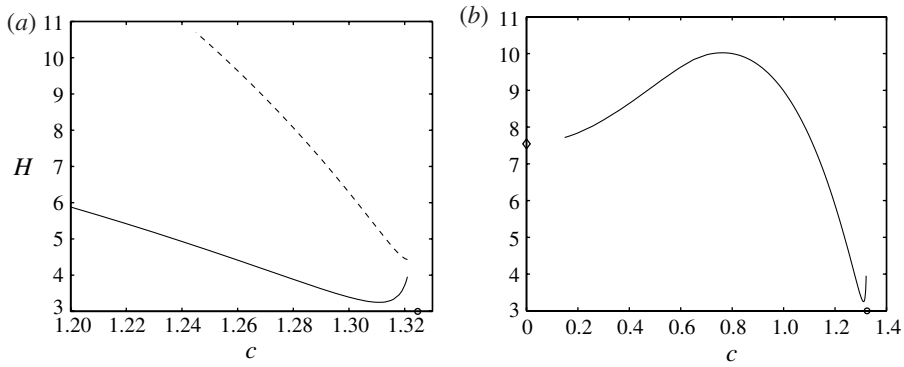

FIGURE 5. (*a*) Energy of the depression solitary wave branch (solid line) and of the elevation branch (dashed line) for $1.2 < c < 1.321$. (*b*) Energy of the entire depression solitary wave branch computed up to the limiting case for $0.15 < c < 1.321$. The value c_{min} is marked by a circle and the energy of the singular solution for $c = 0$ with self-intersecting profile is marked by a diamond.

existence of singular waves with singularities due to self-intersection was discussed by Plotnikov & Toland (2011).

The energy of free solitary waves is given by formula (2.7). The kinetic part can be rewritten in terms of variables at the fluid–ice interface following Longuet-Higgins (1989). In our dimensionless variables, the energy becomes

$$H = -\frac{1}{2}c\int_{-\infty}^{\infty} y\,d\Phi + \frac{1}{2}\int_{-\infty}^{\infty} y^2 x'\,\mathrm{d}\Phi + \frac{1}{2}\int_{-\infty}^{\infty} \frac{(y''x' - x''y')^2}{(x'^2 + y'^2)^{5/2}}\,\mathrm{d}\Phi, \tag{5.2}$$

and it is plotted in figure 5 as a function of the dimensionless velocity c. The most interesting feature is that the energy $H(c)$ has a minimum for the depression branch at $c_m \approx 1.31$. The existence of an extremum for the depression branch suggests an exchange of spectral stability at that point, as shown previously by Saffman (1985) for periodic gravity waves in the full Euler equations, and Akylas & Cho (2008) and Akers & Milewski (2010) for three-dimensional gravity–capillary solitary waves in

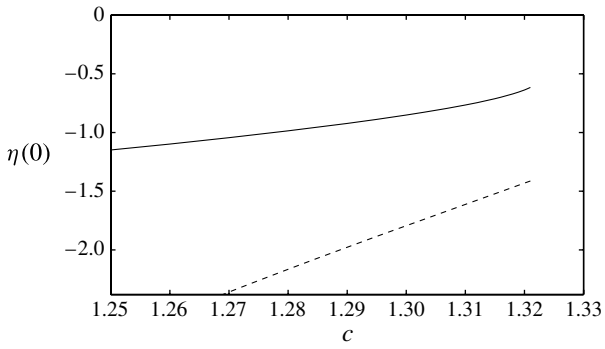

FIGURE 6. Amplitudes of free depression solitary waves for the present Cosserat model (solid line) and for the Kirchhoff–Love model (dashed line).

weakly nonlinear equations. This general property applies to any Hamiltonian system (Saffman 1985). This will be further investigated numerically in the next section using the time-dependent algorithm. The energy decreases monotonically on the elevation branch for values of c up to c_{min} (see figure 5*a*). The energy of waves on the depression branch has also a maximum for $c \approx 0.8$ (see figure 5*b*) but, in that region, the solutions are multivalued and we cannot study their stability with the time-dependent algorithm. The energy of the singular solution for $c = 0$ from figure 4 is also shown (see symbol $\diamond$ in figure 5*b*), and it can be observed that it is the limit for the energy of solitary waves on the depression branch as $c \to 0$.

It is of interest to compare the solitary waves in this case with those obtained when the full flexural pressure term $\kappa_{ss} + (1/2)\kappa^3$ (Cosserat theory) is replaced in (4.15) by the truncated term κ_{xx} (Kirchhoff–Love theory). We have modified our algorithm to compute waves in this simpler case (see Părău & Dias 2002 for an explicit formula for κ_{xx}). In figure 6, we plot amplitudes of depression solitary waves for these two cases. It can be observed that the amplitudes are significantly smaller when the full nonlinear term is considered.

5.2. *Unsteady waves*

We only consider free solitary waves in this section. Solitary waves of depression are first examined. We begin with the situation produced by a small pressure amplitude $P_0 = 0.02$ with $c = 1.3 < c_{min}$. Accordingly, the induced wave is also of small amplitude. Figure 7 confirms the NLS analysis in § 3 that no solitary waves of small amplitude exist. Soon after the pressure is removed at $t = T = 125$, the solution quickly spreads out and no coherent structure is distinguishable.

We now turn our attention to larger amplitudes. It was shown in the previous section that the energy H admits a minimum for $c = c_m \approx 1.31$ along the depression branch, which suggests that such solitary waves are (spectrally) stable for $c < c_m$ and unstable for $c > c_m$. We check this result here with long-time simulations. As indicated in figure 8, the solution generated by $P_0 = 0.1$ and $c = 1.32 > c_m$ is a wavepacket that slowly disperses with time, after the pressure is removed (we chose $T = 125$ in all our computations). The fact that it is a relatively broad wavepacket is related to the proximity to c_{min}, which tends to promote dispersion and thus the instability of the initial localized disturbance. Moreover, the slow decay of this solution is consistent with the choice of c being just slightly larger than c_m.

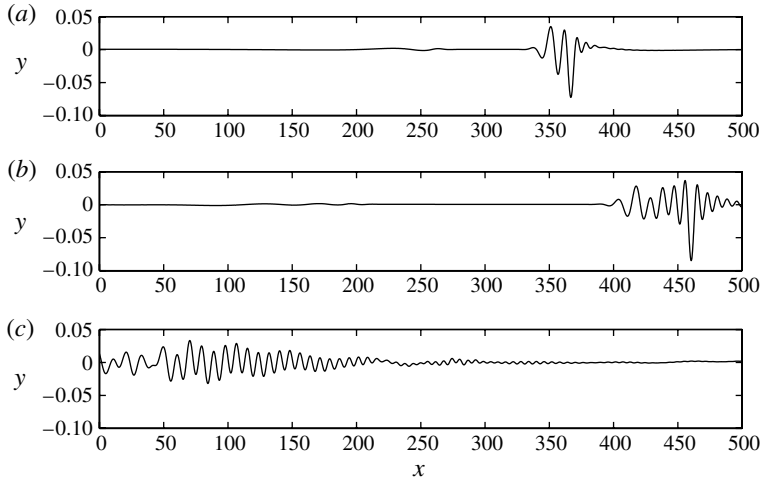

FIGURE 7. Snapshots of the ice-sheet deflection $\eta(x, t)$ at $t = 52$, 123.5, 325 (a–c) for $P_0 = 0.02$ and $c = 1.3$. The pressure is removed at $t = 125$.

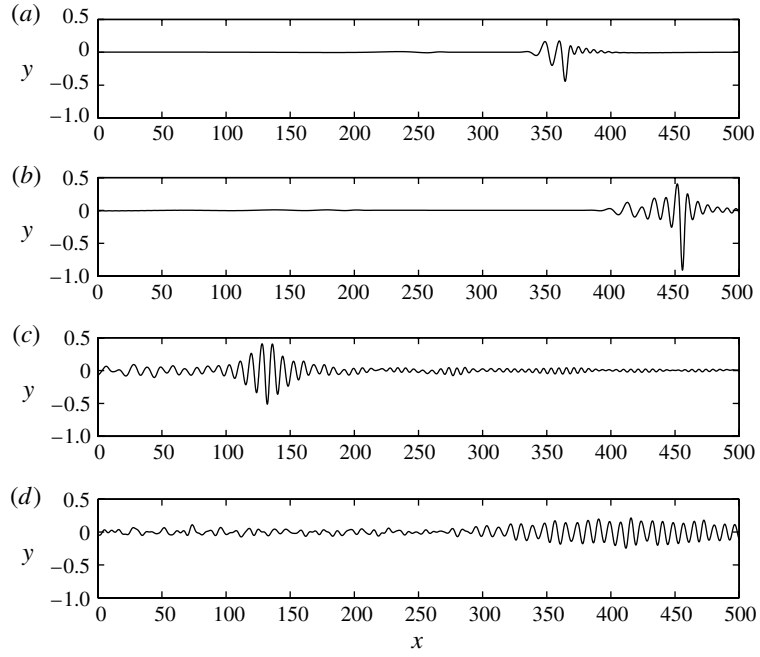

FIGURE 8. Snapshots of the ice-sheet deflection $\eta(x, t)$ at $t = 50$, 120, 330, 1000 (a–d) for $P_0 = 0.1$ and $c = 1.32$. The pressure is removed at $t = 125$.

The next experiment is for $P_0 = 0.3$ and $c = 1.21 < c_m$. In figure 9, we see that the initial disturbance evolves into a stable large-amplitude solitary wave of depression, travelling at near-constant speed with near-constant amplitude at least up to $t = 1000$. This solution is not quite a perfect steadily progressing wave because it constantly

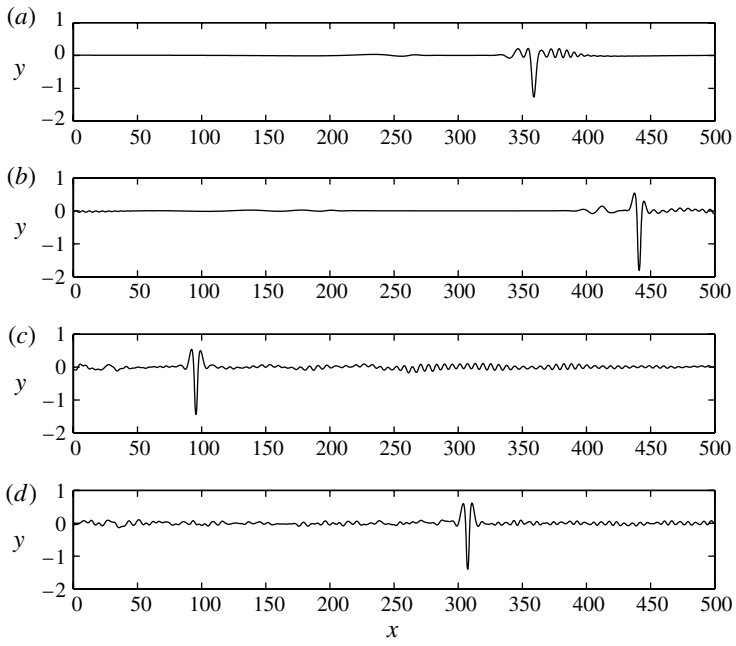

FIGURE 9. Snapshots of the ice-sheet deflection $\eta(x, t)$ at $t = 50$, 120, 330, 1000 (a–d) for $P_0 = 0.3$ and $c = 1.21$. The pressure is removed at $t = 125$.

interacts with the background radiation induced by the initial generation process, as discussed above. Because of the periodic boundary conditions, these small radiative waves remain in the computational domain. We also observe that, for values of c smaller than c_m, there is some sort of relaxation so that the actual speed of the solitary wave measured after $t = T$ is not exactly equal, although close, to the speed initially set by the applied pressure. Distinguishing c, the actual wave speed (by analogy with the steady solutions computed in the previous section), from c_0, the speed of the applied pressure (4.6), we found $c = 1.21$ for the solitary wave in figure 9 while $c_0 = 1.19$.

Incidentally, if the pressure were not removed in the experiment of figure 8 ($P_0 = 0.1$ and $c = 1.32$), this would generate a travelling solitary wave of amplitude ~ -1 and with speed $c \approx 1.27$. For a higher pressure however (say $P_0 = 0.3$), the forced solution would grow in amplitude, leading to computation breakdown after a relatively short period of time. This is consistent with the transcritical regime (i.e. large forcing with speed near c_{min}) as observed by Milewski *et al.* (2011), in which they found no forced travelling waves. A similar instability would also occur if the pressure were constantly applied in the experiment of figure 9 ($P_0 = 0.3$ and $c = 1.21$).

We were not able to compute solitary waves of elevation with our time-dependent scheme, which suggests that the solutions shown e.g. in figure 3 are likely to be unstable. For small (negative) pressure amplitudes, the wave quickly disperses after $t = T$, thus confirming again the NLS analysis presented in § 3. For larger amplitudes however, the initial hump evolves instead into a stable solitary wave of depression. A similar behaviour was observed by Milewski *et al.* (2010) in fully nonlinear computations of gravity–capillary waves. Figure 10 depicts such a solution for $P_0 = -0.6$ and $c_0 = 1.25$. After $t = T$, the wave speed is found to be $c = 1.26$.

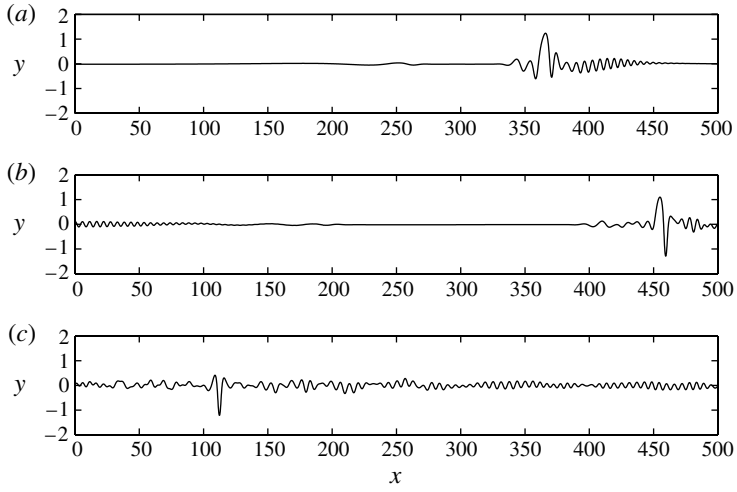

FIGURE 10. Snapshots of the ice-sheet deflection $\eta(x, t)$ at $t = 52, 123.5, 325$ (a–c) for $P_0 = -0.6$ and $c = 1.26$. The pressure is removed at $t = 125$.

This result further supports the fact that large-amplitude solitary waves of depression are stable for $c < c_m$.

Figure 11 shows a direct comparison of wave profiles computed by the boundary-integral method and the high-order spectral method, for various values of c at $t = 289.25 > T$. This comparison may serve as a validation of both methods. In all cases, the agreement is overall very good, especially regarding the location and amplitude of the wave crests and troughs. The discrepancies are mainly attributable to unsteadiness due to interaction with the background radiation.

A comparison of the corresponding spectra is displayed in figure 12. Note that the spectra for $c = 1.28$ and 1.24 are similar, and thus are not shown here for convenience. Because the boundary-integral method solves for $x(\Phi)$ and $y(\Phi)$ with a regular discretization in Φ, this implies that the grid in the physical domain is not necessarily uniform. In order to compute the spectra of steady waves, we first interpolate their profiles at equispaced grid points and then use the fast Fourier transform. We find a good agreement here as well, regarding the overall shape of the spectra. The fact that the graphs for unsteady solutions appear more noisy may be related again to effects of the background radiation. Another observation is that, in all cases, the spectrum is essentially supported within the range $0 < |k| < 3$, with its peak at $|k| \approx 0.75$. As $|k| \to \infty$, the spectrum decays very fast to zero. The typical cut-off wavenumber specified by the ideal low-pass filter in our time-dependent simulations is given by

$$k_c = \nu k_{\max} = \nu \frac{\pi N}{L} \approx 17, \tag{5.3}$$

for $\nu = 0.8$, $N = 4096$ and $L = 600$, which is well beyond the above-mentioned range. This confirms that the filter we used does not significantly affect the unsteady solutions, as pointed out in § 4.2.

Finally, the conservation of the invariants of motion (i.e. energy H, momentum I and volume V) after $t = T$ is illustrated in figure 13, for $c = 1.32$ (figure 8) and $c = 1.21$ (figure 9). In both cases, we see that these quantities are all very well

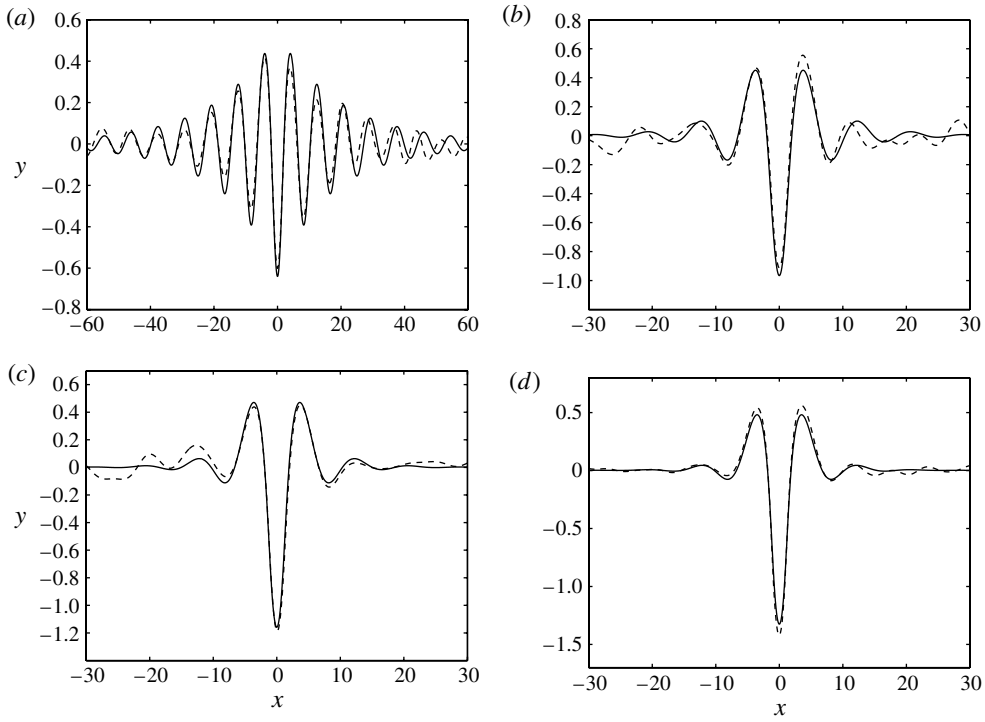

FIGURE 11. Comparison of wave profiles computed by the boundary-integral method (solid line) and the high-order spectral method (dashed line) at $t = 289.25$ for $c = 1.32$, 1.28, 1.24 and 1.21 (a–d).

conserved in time, with V being essentially zero similarly to gravity–capillary solitary waves on deep water (Longuet-Higgins 1989). Comparing figures 5 and 13, we notice that the energy values for $c = 1.32$ (along the depression branch) are both close to $H \approx 4$. However, there is some noticeable difference between $H \approx 6$ from figure 5 and $H \approx 8$ from figure 13 for $c = 1.21$. This may be explained by the more significant contribution of the background radiation to the total energy of the system in the unsteady case with larger wave amplitudes.

6. Conclusions

In this paper, we have investigated two-dimensional nonlinear gravity waves travelling at the interface between an ice sheet and an infinite ocean beneath it. The ice sheet is modelled as a thin elastic sheet according to the special Cosserat theory of hyperelastic shells satisfying Kirchhoff's hypothesis, as derived by Plotnikov & Toland (2011). The resulting mathematical system is conservative and can be written in Hamiltonian form. On this basis, an NLS equation was derived for small-amplitude waves travelling with speeds close to the minimum phase velocity c_{min}. No solitary-wave solutions exist for this NLS equation. However, we expect the situation to change if finite depth is considered. In a related formulation, Părău & Dias (2002) found that the coefficients of their NLS equation change sign above a critical depth. A similar behaviour may happen here, which we plan to investigate in the future.

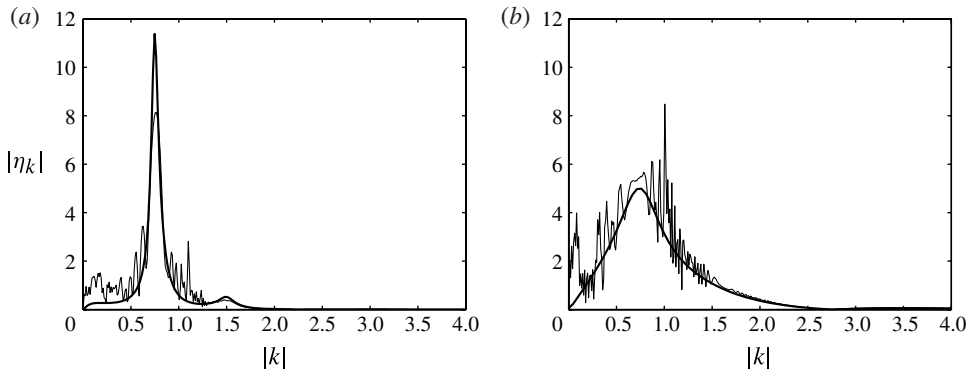

FIGURE 12. Comparison of wave spectra computed by the boundary-integral method (thick solid line) and the high-order spectral method (thin solid line) at $t = 289.25$ for (*a*) $c = 1.32$ and (*b*) $c = 1.21$.

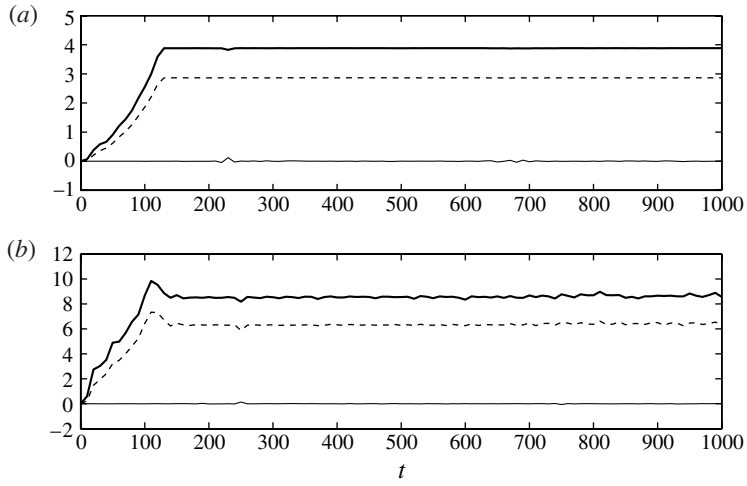

FIGURE 13. Time evolution of energy H (thick solid line), momentum I (dashed line) and volume V (thin solid line) for (*a*) $c = 1.32$ and (*b*) $c = 1.21$. The pressure is removed at $t = 125$.

Steady solutions of the full nonlinear problem were computed in the forced and unforced regimes. Both elevation and depression solitary waves with decaying oscillations were found. As the wave speed approaches c_{min}, the amplitude of solitary waves does not decay to zero, similar to gravity–capillary waves (see Vanden-Broeck & Dias 1992). Limiting waves with overhanging profiles were also calculated for low wave speeds. In the limit $c \to 0$, singular solutions with self-intersecting profiles were obtained.

The energy of depression solitary waves was found to exhibit a minimum at a wave speed c_m slightly less than c_{min}, which suggests that such waves are stable for large amplitudes (i.e. low wave speeds) and unstable for small amplitudes (i.e. high wave speeds). Unsteady computations were also performed and they confirm that there is indeed an exchange of stability for wave speeds close to c_{min}. The other

exchange of stability occurs in regions where the wave profiles become multivalued, which we could not validate with our time-dependent calculations. For elevation waves, their energy was found to decay monotonically as c increases. Time-dependent results suggest that these waves are unstable. Finally, a very good agreement was found when comparing wave profiles of steady and unsteady solutions.

Another planned extension of this study is to investigate three-dimensional solitary waves for the nonlinear hydroelastic model derived by Plotnikov & Toland (2011). The three-dimensional problem was recently addressed by Părău & Vanden-Broeck (2011) in the simplified situation of a linear Euler–Bernoulli plate combined with nonlinear potential flow.

Acknowledgements

P.G. is partially supported by the NSF through grant number DMS–0920850. He also would like to thank the Institute for Advanced Study (Princeton, NJ) for its hospitality during the academic year 2011–2012. E.I.P. is partially supported by the EPSRC under grant EP/J019305/1. Both authors thank the LMS for a Research in Pairs grant.

REFERENCES

AKERS, B. & MILEWSKI, P. A. 2010 Dynamics of three-dimensional gravity–capillary solitary waves. *SIAM J. Appl. Maths* **70**, 2373–2389.

AKYLAS, T. R. 1993 Envelope solitons with stationary crests. *Phys. Fluids* A **5**, 789–791.

AKYLAS, T. R. & CHO, Y. 2008 On the stability of lumps and wave collapse in water waves. *Phil. Trans. R. Soc. Lond.* A **366**, 2761–2774.

BLYTH, M. G., PĂRĂU, E. I. & VANDEN-BROECK, J.-M. 2011 Hydroelastic waves on fluid sheets. *J. Fluid Mech.* **689**, 541–551.

BONNEFOY, F., MEYLAN, M. H. & FERRANT, P. 2009 Nonlinear higher-order spectral solution for a two-dimensional moving load on ice. *J. Fluid Mech.* **621**, 215–242.

CANUTO, C., HUSSAINI, M. Y., QUARTERONI, A. & ZANG, T. A. 1987 *Spectral Methods in Fluid Dynamics*. Springer.

CRAIG, W., GUYENNE, P., NICHOLLS, D. P. & SULEM, C. 2005 Hamiltonian long-wave expansions for water waves over a rough bottom. *Proc. R. Soc. Lond.* A **461**, 839–873.

CRAIG, W., GUYENNE, P. & SULEM, C. 2010 A Hamiltonian approach to nonlinear modulation of surface water waves. *Wave Motion* **47**, 552–563.

CRAIG, W., GUYENNE, P. & SULEM, C. 2012 Hamiltonian higher-order nonlinear Schrödinger equations for broader-banded waves on deep water. *Eur. J. Mech.* B/Fluids **32**, 22–31.

CRAIG, W., SCHANZ, U. & SULEM, C. 1997 The modulational regime of three-dimensional water waves and the Davey–Stewartson system. *Ann. Inst. H. Poincaré (C) Nonlin. Anal.* **14**, 615–667.

CRAIG, W. & SULEM, C. 1993 Numerical simulation of gravity waves. *J. Comput. Phys.* **108**, 73–83.

CRAPPER, G. D. 1957 An exact solution for progressive capillary waves of arbitrary amplitude. *J. Fluid Mech.* **2**, 532–540.

FORBES, L. K. 1986 Surface-waves of large amplitude beneath an elastic sheet. Part 1. High-order solutions. *J. Fluid Mech.* **169**, 409–428.

FORBES, L. K. 1988 Surface-waves of large amplitude beneath an elastic sheet. Part 2. Galerkin solution. *J. Fluid Mech.* **188**, 491–508.

GUYENNE, P. & NICHOLLS, D. P. 2007 A high-order spectral method for nonlinear water waves over moving bottom topography. *SIAM J. Sci. Comput.* **30**, 81–101.

HEGARTY, G. M. & SQUIRE, V. A. 2008 A boundary-integral method for the interaction of large-amplitude ocean waves with a compliant floating raft such as a sea-ice floe. *J. Engng Maths* **62**, 355–372.

KOROBKIN, A., PĂRĂU, E. I. & VANDEN-BROECK, J.-M. 2011 The mathematical challenges and modelling of hydroelasticity. *Phil. Trans. R. Soc. Lond.* A **369**, 2803–2812.

LONGUET-HIGGINS, M. S. 1989 Capillary-gravity waves of solitary type on deep water. *J. Fluid Mech.* **200**, 451–470.

MARKO, J. R. 2003 Observations and analyses of an intense waves-in-ice event in the Sea of Okhotsk. *J. Geophys. Res.* **108**, 3296.

MILEWSKI, P. A., VANDEN-BROECK, J.-M. & WANG, Z. 2010 Dynamics of steep two-dimensional gravity–capillary solitary waves. *J. Fluid Mech.* **664**, 466–477.

MILEWSKI, P. A., VANDEN-BROECK, J.-M. & WANG, Z. 2011 Hydroelastic solitary waves in deep water. *J. Fluid Mech.* **679**, 628–640.

PĂRĂU, E. & DIAS, F. 2002 Nonlinear effects in the response of a floating ice plate to a moving load. *J. Fluid Mech.* **460**, 281–305.

PĂRĂU, E. & VANDEN-BROECK, J.-M. 2011 Three-dimensional waves beneath an ice sheet due to a steadily moving pressure. *Phil. Trans. R. Soc. Lond.* A **369**, 2973–2988.

PLOTNIKOV, P I & TOLAND, J. F. 2011 Modelling nonlinear hydroelastic waves. *Phil. Trans. R. Soc. Lond.* A **369**, 2942–2956.

SAFFMAN, P. G. 1985 The superharmonic instability of finite-amplitude water waves. *J. Fluid Mech.* **159**, 169–174.

SQUIRE, V. A., HOSKING, R. J., KERR, A. D. & LANGHORNE, P. J. 1996 *Moving Loads on Ice Plates*. Kluwer.

TAKIZAWA, T. 1985 Deflection of a floating sea ice sheet induced by a moving load. *Cold Reg. Sci. Technol.* **11**, 171–180.

VANDEN-BROECK, J.-M. 2010 *Gravity–Capillary Free-Surface Flows*. Cambridge University Press.

VANDEN-BROECK, J.-M. & DIAS, F. 1992 Gravity–capillary solitary waves in water of infinite depth and related free-surface flows. *J. Fluid Mech.* **240**, 549–557.

VANDEN-BROECK, J.-M. & PĂRĂU, E. I. 2011 Two-dimensional generalized solitary waves and periodic waves under an ice sheet. *Phil. Trans. R. Soc. Lond.* A **369**, 2957–2972.

XU, L. & GUYENNE, P. 2009 Numerical simulation of three-dimensional nonlinear water waves. *J. Comput. Phys.* **228**, 8446–8466.

ZAKHAROV, V. E. 1968 Stability of periodic waves of finite amplitude on the surface of a deep fluid. *J. Appl. Mech. Tech. Phys.* **9**, 190–194.